



A Model-based dehazing scheme for unmanned aerial vehicle system using radiance boundary constraint and graph model[☆]

Sidharth Gautam^{*}, Tapan Kumar Gandhi, B.K. Panigrahi

Indian Institute of Technology, New Delhi, India

ARTICLE INFO

Keywords:

Remote sensing
Satellite imaging
Unmanned aerial vehicle imaging
Image restoration
Image enhancement
Image dehazing

ABSTRACT

Unmanned aerial vehicle system (UAVs) imaging has become a challenging area of research due to the dynamic atmospheric environment. The images captured by UAVs are often deteriorated by factors such as clouds occlusion, poor atmospheric illumination, and limited capability of the imaging system. To tackle problems, this paper presents a novel visibility restoration scheme for UAVs images by considering the following two assumptions: (1) The actual scene radiance of a UAVs image is bounded. (2) Pixels sharing the same appearance must have the same transmission value in a local neighborhood. Inspired by above assumptions, an image boundary constraint utilizing the median filter has been imposed on the RGB channel for the rough estimation of transmission-map in aerial images. Furthermore, a graph-model based optimization technique has been used for the transmission-map refinement. The experimental results demonstrate the efficiency of the proposed method in terms of metrics correspond to the human-visual-system (HVS).

1. Introduction

The aerial images captured from airplanes or unmanned aerial vehicle system (UAVs) records the ever-changing cultural and natural features on the earth's surface. The aerial images capture several geographical features such as mountains, canyons, flat-lands, and reveal several earth resources such as lakes, rivers, vegetation, mountains, forest, etc. UAVs based imagery provides a valuable source of information for both consumer and computational photography. But unfortunately, these images are often constrained by many negative factors such as occlusion from clouds, poor atmospheric illumination, unpleasant weather conditions, and limited imaging capability of the UAVs. All these undesirable factors play their role collectively, to degrade the colorfulness, sharpness, contrast, and brightness of an aerial image. The visual quality of aerial image plays a crucial role in many types of scientific research and vision-based applications such as surveillance and geospatial mapping [1], city planning, remote sensing, disaster monitoring, agriculture land monitoring [2], and road traffic regulation [3].

In UAVs photography, the atmospheric turbidity varies with altitude, weather, and behavior of suspended particles. However, due to the long distance between the high flying camera and the ground, a significant amount of haze always prevails in the atmosphere. The presence of haze obscure vision to a great extent and degrades the perceptual image quality. The effect of light scattering through haze

particles results in eminent brightness, lessen sharpness, diminished color, and weakened contrast in the captured images. Haze removal, which is also called dehazing, is an integral part of visibility restoration. Over the past decade, significant effort has been made for enhancing the visibility in aerial images. These methods can be divided into two major categories: image enhancement(IE) and image restoration(IR).

In the first category, the most commonly used IE methods are based on the advanced histogram equalization and its variants [4,5], retinex theory [6,7], gamma correction [8], nonlinear intensity transformation function (NIT) [9], and wavelet analysis [10]. As color, contrast and brightness are important visibility factors in aerial images, Fu et al. [5] improved visibility by maximizing the image colorfulness, contrast, and minimizing the brightness using regularized-histogram-equalization and discrete-cosine-transform (RHE-DCT). The results are visually compelling but dark and saturated in some local regions of the image. Jang et al. [6] developed a method based on sub-band decomposed multiscale retinex with hybrid intensity transfer function to improve the visibility in remote sensing satellite and aerial images. Yong et al. [10] used the wavelet transform to decompose haze into different spatial layers. This technique requires an additional haze-free image of the same scene as a reference for efficient dehazing. Therefore, it cannot be used when a single aerial image is available as an input. In contrast, Kwok et al. [11] used a series of independent filters to improve colors, saturation, and contrast in aerial images. This method produces

[☆] This paper has been recommended for acceptance by Zicheng Liu.

* Corresponding author.

E-mail address: sidharthgautam02@gmail.com (S. Gautam).

results with vivid colors and sharp object boundaries, but using too many filters on one image is computationally intensive and often results in unnatural-looking images. Sidike et al. [12] used adaptive trigonometric transformation function (i.e., ATTF) for visibility enhancement in aerial images, but it mostly causes over-saturation.

The IE methods [4–12] fails to consider the absorption and scattering effects of the atmosphere. Therefore, they often result in color distortion and over-saturation, as they are unable to maintain the color fidelity under cloudy or smoky conditions. In short, IE methods are not sufficient enough for dehazing as they were developed for enhancement only. Limitations of the IE methods [4–12] motivate the researchers to develop new IR approaches. In contrast to IE, the IR methods first study the optical process of image formation under the atmospheric imaging model and make use of priors, assumptions, and constraints for the visibility recovery.

In the IR category, the majority of methods are based on simple yet effective, dark channel prior (i.e., DCP), proposed by He et al. [13]. In [14], Long et al. performed the dehazing of remote sensing images by using the DCP and low pass Gaussian filter. In [15], Cheng et al. combined the DCP with a guided filter for the dehazing of an aerial image. In [16], Singh et al. combined the DCP with fourth-order partial differential equations based trilateral filter (FPDETF) to restore the visibility in satellite images. Similarly, Huang et al. [17] used DCP under layered scattering framework to restore visibility in remote sensing images. The DCP based dehazing techniques [13–17] are visually compelling, but they are likely to introduce artifacts, especially when DCP assumptions fail for the white and sky-regions in aerial images.

To overcome the shortcomings of DCP, Zhao et al. [18] improves the DCP with a bright region filling process to alleviate the color distortion in aerial images. Similarly, Carr and Hartley [19] improved the DCP with a piece-wise planar geometry prior using the energy minimization framework. Zhu et al. [20] used a machine learning approach to model the scene-depth and created color attenuation prior (i.e., CAP) for the rough estimation of depth-map. Berman et al. [21] proposed a non-local method for dehazing. Bui et al. [22], introduced color ellipsoid prior for dehazing. Unlike the above methods, which use different priors for dehazing, Meng et al. [23] developed BCCR, that uses weighted L1-norm based contextual regularization to recover the unknown transmission-map in hazy images.

Recently, there has been a flurry of works that utilize neural networks, deep learning frameworks, and hybrid methods [24–30] to learn the transmission-map directly from the training data. Tang et al. [24] used haze relevant features such as dark channel, hue disparity, local max saturation, and local max contrast in a random-forest framework to learn the transmission-map. Cai et al. [25] presented dehazenet, which is an end-to-end trainable system that uses CNNs and BReLU for the transmission-map estimation. Similarly, Ren et al. [26] presented a multi-scale convolutional neural network (MSCNN) that comprises of a coarse-scale network to predict the transmission-map in haze images, and a fine-scale network to obtain the detailed transmission-map. Recently, Li et al. [27] proposed an all-in-one dehazing network called AOD-Net, which can jointly learn the transmission-map, and air-light for dehazing. Likewise, Zhang et al. [28] proposed a densely connected pyramid dehazing network (DCPDN), which can be jointly optimized to learn the transmission-map, atmospheric light, and dehazing all together. More recently, Yang et al. [29] introduced a learning-based deep network called proximal dehaze-net for dehazing. In [30], Du et al. propose a novel deep residual learning (DRL) network for dehazing.

Besides the above dehazing methods, many other interesting algorithms presented in [31–35] have shown significant advantages for dehazing terrestrial images. Despite the remarkable progress in dehazing, there is still room for improvement, especially in terms of the quality measure. This paper presents an assumption based novel visibility restoration scheme for UAVs images. The contributions of the paper are the following:

1. By considering the first assumption, boundary constraint utilizing the median filter has been imposed on the RGB color channel for the rough estimation of transmission-map in UAVs images.
2. Inspired by Closed-matting [36] and KNN-matting [37], both local and non-local information has been used, collectively, in the second assumption for the refinement of transmission-map using a graph model.
3. To solve the color-cast problem, a color correction approach based on the gray-world assumption has been used while recovering the scene radiance.

The remainder of this paper is organized as: In Section 2, a brief background of the ‘atmospheric imaging model’ and ‘dark channel prior (DCP)’ is presented. Section 3, outlines some of the major limitations of DCP for UAVs images. Section 4, describes the proposed approach in detail. Experimental results are shown in Section 5. Finally, a conclusion is drawn in Section 6.

2. Problem formulation and motivation

2.1. Atmospheric imaging model

The imaging model widely used to describe the formation of haze images [13–22] is expressed as:

$$I(x) = J(x)t(x) + A(1 - t(x)) \quad (1)$$

$$t(x) = e^{-\beta d(x)} \quad (2)$$

where, $I(x)$ is the intensity of an observed image degraded by haze, $J(x)$ is the radiance of a haze-free image, A is the global air-light, $t(x) \in [0, 1]$ is the medium transmission-map, (β) is the attenuation coefficient of the atmosphere and $d(x) \in [0, \infty)$ is the scene-depth or distance from the camera to the scene being targeted. On putting the value of $t(x)$ into Eq. (1):

$$I(x) = J(x)e^{-\beta d(x)} + A(1 - e^{-\beta d(x)}) \quad (3)$$

In Eq. (3), the term $J(x)e^{-\beta d(x)}$ is called the direct attenuation, which indicates the amount of attenuation that actual scene radiance faces before reaching the camera. The term $A(1 - e^{-\beta d(x)})$ is called the local air-light, which fades the color and adds whiteness in the scene. It is worth noting, for homogeneous weather (β) is treated as a constant and $d(x)$ becomes the most important term for the transmission-map estimation. Moreover, in the ideal case, the range of $d(x)$ is $[0, +\infty)$ as the UAVs can be either very close or too far from the target object. Considering Eq. (3), when the distance between the scenery object and the camera is higher, the observed image is dominated by the air-light as:

$$I(x) = A, \quad \text{when } d(x) \rightarrow \infty, \quad t(x) \rightarrow 0 \quad (4)$$

Similarly,

$$I(x) = J(x), \quad \text{when } d(x) \rightarrow 0, \quad t(x) \rightarrow 1 \quad (5)$$

Eq. (4) implies that when a scenery object exists at a large distance from the UAVs camera ($e^{-\beta d(x)} \approx 0$), the observed image (I) is the most haze-opaque due to the stronger air-light effect. Likewise, Eq. (5) implies that for short distance objects, the observed image is nothing but the actual scene radiance, and does not require any dehazing. Practically, both the scenario given by Eqs. (4) and (5) are not possible in aerial imaging. Therefore, we need to compute both A and $t(x)$ independently, to recover the actual scene radiance $J(x)$. In order to simplify this ill-posed inverse problem, it is essential to consider some constraints, priors, and assumptions.

2.2. Dark channel prior

The DCP [13] is based on the property of “dark pixels”, which have a very low intensity in at least one color channel of an outdoor haze-free image. Mathematically, the DCP for a haze-free image $J(x)$ is given by:

$$J^{Dark}(x) = \min_{y \in \Omega_r(x)} \left(\min_{c \in \{r,g,b\}} J^c(y) \right) \quad (6)$$

where $\Omega_r(x)$ is an image $(r \times r)$ local patch centered at pixel x , and \min is a minimum filter. For the estimation of transmission-map $\hat{t}(x)$, it is assumed that the air-light (A) is known and Eq. (1) is normalized by the air-light (A) as:

$$\frac{I^c(x)}{A^c} = \frac{J^c(x)\hat{t}(x)}{A^c} + 1 - \hat{t}(x) \quad (7)$$

On applying DCP [13] on both sides of Eq. (7):

$$\min_{\Omega_r} \left(\min_c \left(\frac{I^c(x)}{A^c} \right) \right) = \min_{\Omega_r} \left(\min_c \left(\frac{J^c(x)}{A^c} \right) \right) \hat{t}(x) + 1 - \hat{t}(x) \quad (8)$$

Accordingly DCP [13], the dark channel of haze-free image $J(x) \approx 0$:

$$\min_{\Omega_r} \left(\min_c \left(\frac{J^c(x)}{A^c} \right) \right) = 0 \quad (9)$$

After putting Eq. (9) into Eq. (8), $\hat{t}(x)$ is given by:

$$\hat{t}(x) = 1 - w \left\{ \min_{\Omega_r} \left(\min_c \left(\frac{I^c(x)}{A^c} \right) \right) \right\} \quad (10)$$

Unfortunately, the results may appear artificial when haze is removed completely. Thus He et al. [13] adds a constant $w(0 < w \leq 1)$ in Eq. (10) to preserve little haze for distant objects. The $\hat{t}(x)$ estimated by Eq. (10) is further refined as optimal transmission $t(x)$ through a filtering technique [36]. Finally, the scene radiance $J(x)$ is recovered via:

$$J^c(x) = \frac{I^c(x) - A^c}{\max\{t(x), 0.1\}} + A^c, \quad c \in \{r, g, b\} \quad (11)$$

For avoiding division by zero, He et al. [13] restricted the value of the transmission-map $t(x)$ by 0.1.

3. Limitations of DCP for UAVs image

Despite the good performance for dehazing outdoor images, the DCP show limitations for the UAVs images as:

3.1. Inefficient transmission estimation

Due to the use of \min operator in Eq. (10), a lower intensity value indicates that the captured area contains thin haze, Conversely, a higher value indicates thick haze. However, this is not true for UAVs haze images. Actually, in aerial images, due to the long distance between the camera and the scene, the intensity of the red color channel is attenuated much faster than the green and blue channel. Therefore, a lower intensity in the red channel may mislead the DCP to perceive a thin haze layer in aerial images, which is not true. Furthermore, when the intensity of any bright object in aerial images $I(x)$ becomes similar to the intensity of air-light (A) then, according to Eq. (10):

$$\min_{\Omega_r} \left(\min_c \left(\frac{I^c(x)}{A^c} \right) \right) \rightarrow 1 \quad \text{and} \quad \hat{t}(x) \rightarrow 0 \quad (12)$$

Eq. (12) implies that DCP fails to obtain the estimation of scene transmission-map, which is the key to efficient dehazing.

3.2. Color distortion

The UAVs haze images usually exhibit different color distortion in their RGB histogram, due to the long distance between the camera and the scene. Fig. 1 shows the histogram distributions of natural scene images and UAVs haze images. Intuitively, the histogram distributions of a natural-scene image are consistent and wider while the histogram

distributions of UAVs haze images are inconsistent (e.g., the histogram of the red channel shifted towards the darkest side, followed by the blue channel and then green channel). It happens because the red color of the spectrum has the longest wavelength, causing it to be scattered and absorbed extensively by atmospheric particles, while the blue color wavelength is comparatively shortest, causing it to travel the maximum distance in the air. Therefore, UAVs images often show a bluish-greenish tone. However, owing to use an assumption in DCP [13] that each color channel of the input image has similar color distributions in their histogram, the UAVs images features serious color-shift problem, when the same restoration scheme given in Eq. (11) used for each color channel. The histogram distribution of UAVs images inspires us to re-structure Eq. (11) to achieve better results.

4. Proposed scheme

The proposed method is based on the following two assumptions: (1) The actual scene radiance of an aerial image is always bounded such that the intensity of each color channel falls in the range $[C_0 \leq J^c(x) \leq C_1]$; (2) Pixels sharing the same appearance must have the same value in the transmission-map (i.e., $t(x)$ is locally constant).

4.1. Estimation of air-light

Air-light fades the colors due to the addition of whiteness in the scene and its effect varies sharply along with the distance between the UAVs camera and the ground scenery object. In UAVs imaging, Eqs. (4) and (5) implies that the influence of air-light is stronger in the regions of deeper-depth and weaker in the region of shallow-depth. Since the air-light contribution increases with the increment in scene-depth, its value can be estimated by detecting the farthest pixel in the haze-opaque regions of the image. In other words, pixels belonging to the haze-opaque regions are often identified as the brightest ones and contains a fair amount of air-light (A) as:

$$A^c = I^c \left(\arg \max_{x \in P_{0.1}} \left(\min_{y \in \Omega_r(x)} \left(\min_{c \in \{r,g,b\}} I^c(y) \right) \right) \right) \quad (13)$$

In Eq. (13), the air-light contribution is determined by selecting the pixels corresponding to the top 0.1% of brightest pixels in the dark channel of an aerial image. Then among these brightest pixels, the one corresponding with the highest intensity in the aerial image (I) is chosen to provide the estimation of air-light. However, this approach is not suitable in a situation where scenery objects are brighter than the air-light. Fig. 2 shows an example of global air-light estimation.

4.2. Boundary constraint for transmission estimation

Under aerial imaging, Eq. (4), implies that the intensity of pixel $I(x)$ belonging to the region with a distant view will be pushed towards air-light (A). Therefore, in order to find an initial estimation of transmission-map $\hat{t}(x)$ for any pixel (x) , the main requirement is the extrapolation of $J(x)$ which cannot cross over the boundary of RGB color channel and must be located within C_0 and C_1 . So, Eq. (1) can be rewritten as [38]:

$$J_b(x) = \frac{I(x) - A(1 - t(x))}{t(x)} \quad (14)$$

Now, by considering our first assumption that actual scene radiance of a haze image is always bounded such that the intensity of each color channel falls in the range $[C_0 \leq J^c(x) \leq C_1]$, where C_0 and C_1 are two constant vectors relevant to the input image. Furthermore, to simplify the calculation procedure, the intensity of each color channel is normalized within $[0, 1]$, which in turn, imposes the boundary constraint on Eq. (14) as:

$$0 \leq \frac{I^c(x) - A^c(1 - t(x))}{t(x)} \leq 1 \quad (15)$$

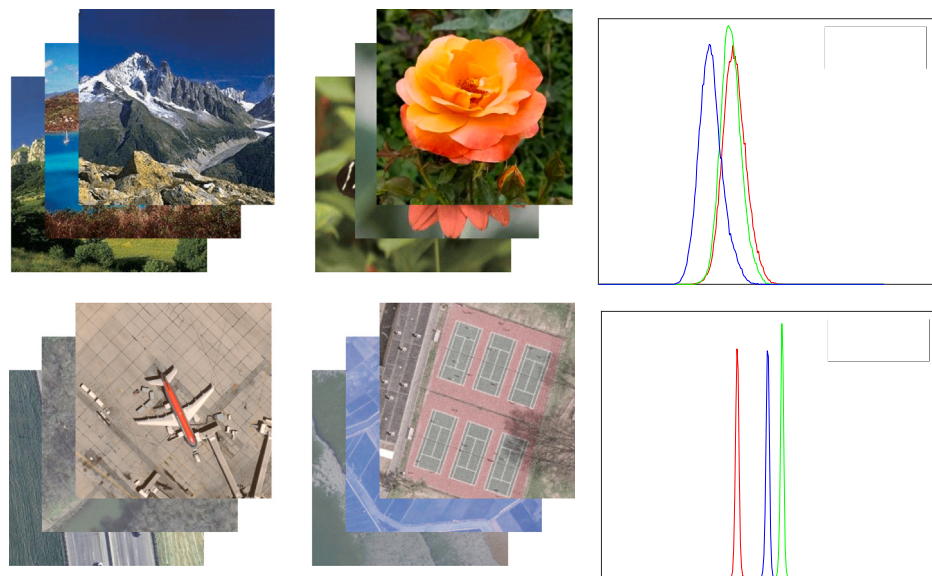


Fig. 1. Statistical difference between a terrestrial image dataset and UAVs image dataset. Top row: Terrestrial image dataset and it's average histogram distribution. Bottom row: UAVs image dataset and it's average histogram distribution. (For interpretation of the references to colour in this figure legend, the reader is referred to the web version of this article.)

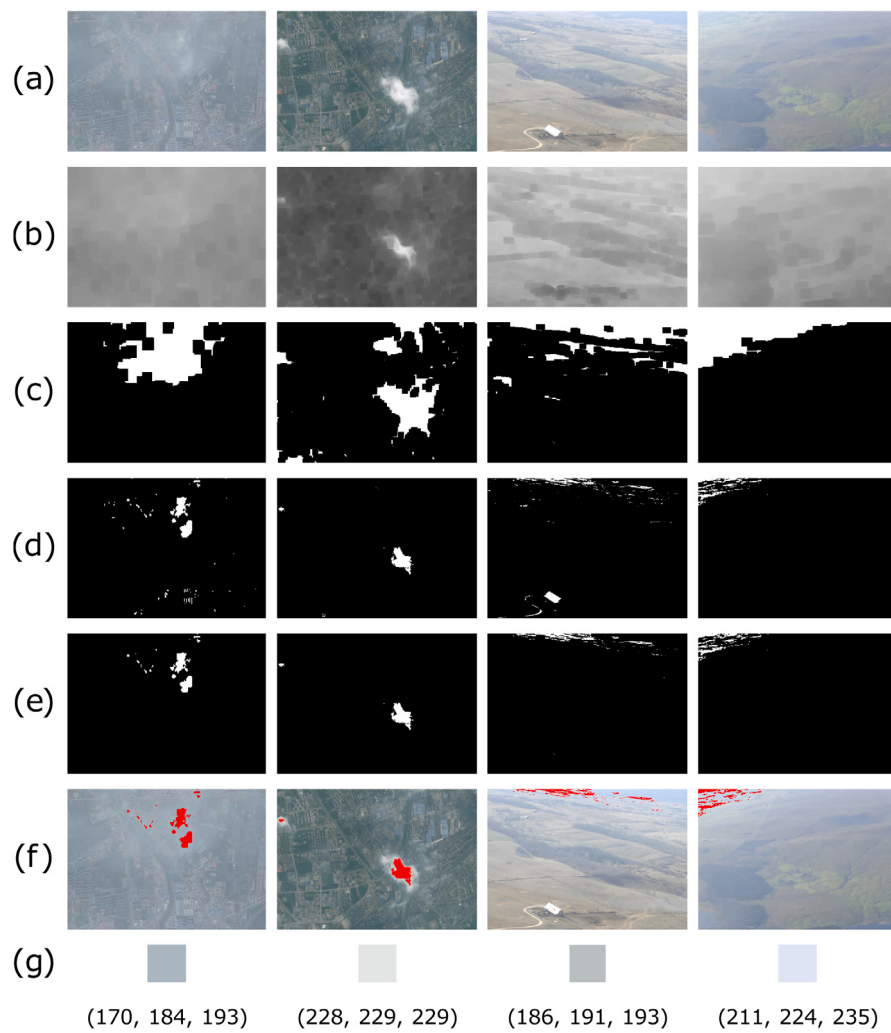


Fig. 2. An example to illustrate the global air-light estimation. (a) Real UAVs haze images. (b) Corresponding Dark channels. (c) The top 0.1% of brightest pixels in the dark channels. (d) The top 0.1% of brightest pixels is used as the threshold Δ to obtain dark channel mask. (e) Logical AND of (c)–(d) images to identify most haze-opaque pixels. (f) Pixels mapped to the input image for air-light estimation. (g) Estimated air-light.

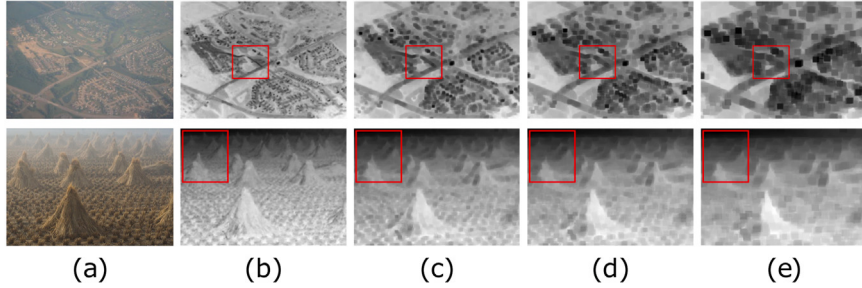


Fig. 3. Illustration of the effect of patch variation while estimating the transmission-map for haze images. (a) UAVs haze image (top) and terrestrial haze image (bottom). The transmission-map derived by Eq. (18) with the patch size of (b) $\Omega = 5$ (c) $\Omega = 11$ (d) $\Omega = 15$ (e) $\Omega = 21$.

The solution of Eq. (15) results in the two inequations as:

$$t_1(x) \geq 1 - \frac{I^c(x)}{\max(A^c, \Phi)} \quad \text{and} \quad t_2(x) \geq \frac{I^c(x) - A^c}{1 - A^c} \quad (16)$$

where Φ is a small constant to avoid division by zero and A^c is the known air-light for each color channel. Based on the above mentioned solution, the initial estimation of the transmission-map $t_i(x)$ can be given by:

$$t_i(x) = \max\{t_1(x), t_2(x)\} \quad (17)$$

To sum up, the initial transmission of the whole image, the transmission value for each pixel in a local neighborhood is calculated by processing an initial estimate as:

$$\hat{t}(x) = \text{med}_{y \in \Omega_r(x)} \left(\max_{z \in \Omega_r(y)} (t_i(z)) \right) \quad (18)$$

where $\Omega_r(x)$ and $\Omega_r(y)$ represent an image $(r \times r)$ local patch centered at pixel location x and y , respectively. med and \max denote the operator of a median and maximum filter, respectively. The use of med operator in Eq. (18) avoids to decrease the perceptible resolution sharply and performs a non-linear filtering operation, which not only suppresses the impulsive noise components but also preserves the edge information while estimating the scene transmission-map.

In Eq. (18), the size of the local patch (Ω) is the only parameter that needs to be determined for the estimation of a stable transmission-map. Although the effect of the size of the local patch is significant, a large patch-size unnecessarily increases the computational-time and makes the block-artifact stronger near depth jumps, while a smaller patch-size could make the dehazing results over-saturated [13]. The impact of variation of the patch-size on the estimation of $\hat{t}(x)$ is shown in Fig. 3. The top row of Fig. 3(a), corresponds to an aerial image with less local-texture and dense haze. Therefore, a medium-patch is sufficient in order to well estimate the foreground and background regions in the $\hat{t}(x)$. However, a terrestrial image with complicated local-texture and mild haze, shown in the second row of Fig. 3(a), needs a larger-patch to avoid the false estimation of these regions. It can be observed from Fig. 3(e), that terrestrial image regions (i.e., the foreground and background) remain visible even when a large-patch ($\Omega = 21$) is used whereas, UAVs image regions deteriorated for the same patch size. Therefore, a reasonable value of patch-size (Ω) needs to be found for UAVs dehazing.

4.3. Graph model for transmission-map refinement

The transmission-map $\hat{t}(x)$ obtained by Eq. (18) is called tri-map because it contains three class of regions. It can be observed from Fig. 3[(b)-(e)], especially in the boundary marked by the red color that three classes of regions exist in $\hat{t}(x)$. The foreground region (indicated by lighter pixels), the background region (indicated by darker pixels), and unknown region (indicated by gray pixels). If we try to recover the scene radiance $J(x)$ directly using $\hat{t}(x)$, the results feature problems such as false textures and block-artifacts. Hence, it is necessary to refine the $\hat{t}(x)$ to obtain a smooth and sharp transmission-map.

The method used for refinement of $\hat{t}(x)$ is motivated by the assumption that pixels sharing the same appearance must share the same transmission value [37]. Using this assumption, the unknown-region in $\hat{t}(x)$ can be partitioned into a known foreground (F), and known background (B) by using the proposed graph model. The illustration of the graph model is shown in Fig. 4 where red, blue, and gray nodes represent pixels marked by tri-map as foreground, background, and unknown, respectively. In the tri-map $\hat{t}(x)$, the transmission value for unknown pixels may reflect the tendency towards either foreground or background. Thus it is reasonable to associate a confidence value (γ) to indicates whether a pixel belongs to the foreground or background. The data weights for unknown pixel (x) are defined as:

$$w_{x,F} = \gamma \cdot \hat{t}(x) \quad \text{and} \quad w_{x,B} = \gamma \cdot (1 - \hat{t}(x)) \quad (19)$$

where $w_{x,F}$ and $w_{x,B}$ define the probability of pixel belonging to the foreground and background. Eq. (19) implies that a true foreground pixel must have a higher value of $w_{x,F}$ and lower value of $w_{x,B}$, and vice-versa. Furthermore, to enforce smoothness, each pixel is connected to the local neighbor (w_{spa}) [36], non-local neighbor (w_{knn}) [37], virtual foreground (Ω_F) and to the virtual background (Ω_B) (see Fig. 4(b)) through the use of a weighting function given by:

$$w_{xy} = w_{spa}(x, y) + w_{knn}(x, y) + w_{x,F} + w_{x,B} \quad (20)$$

$$w_{spa}(x, y) = \sum_{k|(x,y) \in \Omega_k} \left(\delta_{xy} - \frac{1}{|\Omega_k|} \left(1 + (I_x - \mu_k)^T \times \left(\Sigma_k + \frac{\epsilon}{|\Omega_k|} U_3 \right)^{-1} (I_y - \mu_k) \right) \right) \quad (21)$$

where y is a neighbor of x , $|\Omega_k|$ is the number of pixels in a local-patch, μ_k and Σ_k are the colors mean and variance in a window (Ω_k), δ is Kronecker's delta function, U_3 is the 3×3 identity matrix, and ϵ is a small regularization parameter to control the strength of smoothness. Furthermore, due to the long distance from the ground, aerial images usually have an overlapped area of color-distribution. Therefore, to solve this problem, a multi-dimensional feature space has been used, which uses spatial and edges variations as an additional feature to color [39] as:

$$F_x = [h \ s \ v \ p \ q \ |I_p| \ |I_q| \ |I_{pp}| \ |I_{qq}|]_x \quad (22)$$

where F_x represents a 9-dimensional feature vector of pixel x , $I = [h, s, v]$ represents the pixel value in the HSV color space, $(p, q \in x)$ represents the pixel location. I_p , I_q , I_{pp} , and I_{qq} represent the first and second-order derivative of the image intensity in the horizontal and vertical directions. To enforce the inter-region smoothness in $\hat{t}(x)$, pixel x is connected to K -nearest neighbors y_1, y_2, \dots, y_k in the high dimensional feature space with weights $w_{knn}(x, y)$ as:

$$w_{knn}(x, y) = 1 - \frac{\sum_{x=1}^N \|F_x - \sum_{m=1}^K F_{ym}\|}{\sigma} \quad (23)$$

where N is the total number of pixels in the image, and σ is the least upper bound of $\sum_{x=1}^N \|F_x - \sum_{m=1}^K F_{ym}\|$ to constraint the value

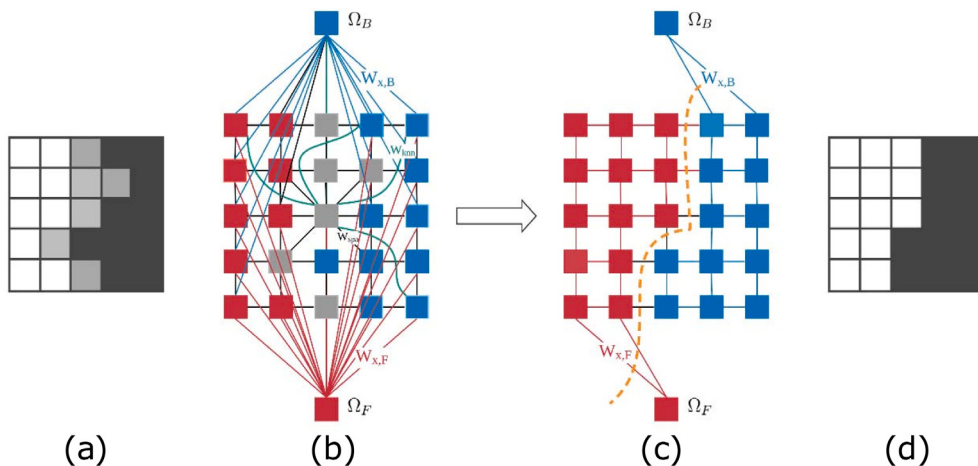


Fig. 4. Illustration of transmission-map refinement using the graph model. (a) Tri-map replica. (b) Graph model before optimization. (c) Graph model after optimization. (d) Filtered tri-map replica. (For interpretation of the references to colour in this figure legend, the reader is referred to the web version of this article.)

of $w(x, y)$ in $[0,1]$. The refined transmission-map $t(x)$ is obtained by minimizing the following cost function [40].

$$E = \lambda \sum_{x \in v} (t_x - \hat{t}_x)^2 + \sum_{x=1}^N \left(\sum_{y \in N_x} w_{xy} (t_x - \hat{t}_x)^2 \right) \quad (24)$$

where v is the set of definite foreground and background pixels, \hat{t} is the estimated transmission-map (i.e. Tri-map). In Eq. (24), the first term ensures that the refined transmission-map is consistent with the constraint of estimated transmission-map, whereas the second term ensures that neighboring pixels share similar transmission values, λ is a parameter to keep the balance between the two terms. To facilitate computation, Eq. (24) can be further rewritten in matrix form as:

$$E = \lambda (t - \hat{t})^T \Gamma (t - \hat{t}) + t^T L^T L t \quad (25)$$

where,

$$L_{xy} = \begin{cases} w_{xx} & \text{if } x = y \\ -w_{xy} & \text{if } x \text{ and } y \text{ are neighbors} \\ 0 & \text{otherwise} \end{cases}$$

where $w_{xx} = \sum_{y \in N_x} w_{xy}$, Γ is a $N \times N$ diagonal matrix with $\Gamma_{xx} = 1$ if $x \in v$, else 0. The solution to Eq. (25) can be given by solving the following sparse linear system:

$$t = (L^T L + \lambda U)^{-1} \hat{t} \quad (26)$$

where U is an identity matrix, \hat{t} is the estimated tri-map, and λ is a parameter which controls the smoothness of data term. Fig. 5 shows an example of graph-model based refinement. The irregularities formed while estimating the transmission are suppressed and smoothed out, effectively, which leads to the recovery of high-quality transmission-map.

4.4. Recovery of scene radiance using color correction

Unlike terrestrial images, UAVs haze images usually suffer from color-distortion due to their long distance from the ground and unfavorable lightening conditions. The color-distortion severely affects the visual quality of aerial images. Therefore, to solve this problem, a color correction technique based on statistical approach is adopted by modifying Eq. (11) as [42]:

$$J^c(x) = \frac{I^c(x) - (A^c - \Psi^c(x))}{[\max\{t(x), t_0\}]^\beta} + (A^c - \Psi^c(x)) \quad (27)$$

$$\Psi^c(x) = \operatorname{argmax}[\bar{I}^c(x)] - \bar{I}^c(x) \quad (28)$$

where (A) is the estimated air-light, $t(x)$ is the filtered transmission-map, $\Psi^c(x)$ denotes the color difference value between the maximum mean intensity and the mean intensity of red, green, and blue channel of image (I). In other words, due to the longer distance between the camera and the scene, the offset for each color channel is subtracted for the recovery of actual scene radiance. For avoiding division by zero, the value of the transmission-map $t(x)$ is restricted by t_0 . An example of radiance recovery using the proposed approach is shown in Fig. 5.

5. Experimental results

In this section, we examine the effectiveness of the proposed method on both realistic [41,43,44] and synthetic dataset [45] and compare its performance against state-of-the-art methods.

5.1. Datasets

The experiments of the proposed method are carried out on both realistic and synthetic dataset. The real UAVs haze images are sourced from the database of QUICK-BIRD satellite [41], PLEIADES satellite [43], and USC-SIPI dataset [44]. The QUICK-BIRD and PLEIADES satellite dataset contain a wide range of aerial images with a spatial resolution of 5980×2774 , 2624×1098 , and 3535×1640 pixels respectively, whereas the USC-SIPI dataset contains bluish-cast haze images with a spatial resolution of 512×512 , 1024×1024 , and 2250×2250 pixels. In this paper, the UAVs test images are generated from cropping different haze regions from the real dataset and resized to 512×512 . The synthetic haze images are sourced from RESIDE- β dataset [45]. In RESIDE- β dataset [45], several images with variable haze thickness are synthesized using Eq. (1) by randomly chosen air-light from $[0.7, 1.0]$ and β between $[0.6, 1.8]$ since any value of β beyond this range could lead to unrealistic haze (too thin or too heavy).

5.2. Parameter setting

The proposed dehazing scheme consists of few parameters and constants. Therefore it is necessary to investigate the impact of those parameters for transmission-map estimation, transmission-map refinement, and radiance recovery. To evaluate the impact of patch-size (Ω), a set of experiments has been carried out using different values of this parameter. The experimental results are shown in Fig. 3, where a small patch-size ($\Omega = 5$) leads to the under-estimation of transmission-map (see Fig. 3(b)), while a large-patch ($\Omega = 21$) leads to the over-estimation of transmission-map (see Fig. 3(e)). It is important to note that when the patch size is too small, the assumption of constant

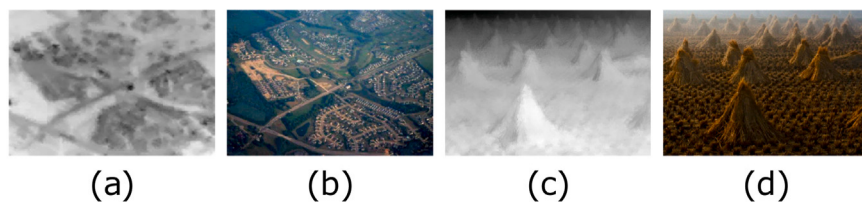


Fig. 5. An example of transmission-map refinement and radiance recovery using the proposed approach. (a) and (c) Filtered transmission map derived from images shown in Fig. 3(d). (b) and (d) Final dehazing results.

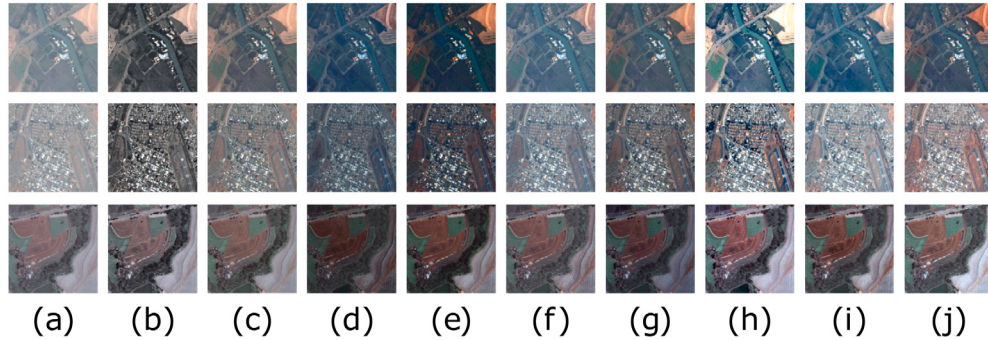


Fig. 6. Qualitative comparison with other state-of-the-art methods on QUICK BIRD dataset [41]. (a) Satellite haze images. (b) Fu et al. [5] (c) Kwok et al. [11] (d) He et al. [13] (e) Zhu et al. [20] (f) Meng et al. [23] (g) Cai et al. [25] (h) Zhang et al. [28] (i) Yang et al. [29] (j) Proposed method (Please zoom-in for better illustration of minor details). (For interpretation of the references to colour in this figure legend, the reader is referred to the web version of this article.)

transmission becomes less appropriate. On the other hand, a large patch-size, unnecessarily increases the computational time and makes the halos-artifact stronger near depth edges. It can be seen in Fig. 3[(c)–(d)], that the best estimation of foreground and background regions is achieved for a medium patch-size. However, the parameters (Ω) are data driven, but ($\Omega = 15$) is used for all results reported in this paper. For tri-map refinement, the constants remain same irrespective of the image under restoration and a fixed value of $\gamma = 0.1$, $K = 12$, $\epsilon = 10^{-6}$, $\lambda = 10^{-4}$ is used. Furthermore, the parameter t_0 and δ in Eq. (27) is fixed to 0.3 and 0.85 for fine detailing of dehazing effect. For fair comparisons, we use the provided codes of state-of-the-art-methods [5,11,13,20,23,25,28,29] and set the parameters optimal as suggested by authors to generate the final dehazing results.

5.3. Qualitative comparison on real UAVs images

The qualitative comparison of proposed method with other state-of-the-art methods on real UAVs images are shown in Figs. 6–8. For qualitative evaluation, we randomly chose three realistic haze images from each UAVs dataset, as shown in Figs. 6(a)–8(a). The dehazing result of Fu et al. [5], Kwok et al. [11], He et al. [13], Zhu et al. [20], Meng et al. [23], Cai et al. [25], Zhang et al. [28], and Yang et al. [29] are given in Fig. 6[(b)–(i)] to Fig. 8[(b)–(i)], respectively. The results of the proposed method are given in Figs. 6(j)–8(j). Among these results, Cai et al. [25], Zhang et al. [28], and Yang et al. [29] methods are based on deep learning.

The reader is urged to zoom into the results to view the images more clearly in Figs. 6–8. Upon zooming, one can observe, most of the haze effects are removed by [5,11,13,20,23,25,28], and [29], respectively. However, visibility, colors, and details are not good enough. It can be seen in Figs. 6(b)–8(b), that Fu et al. [5] results are over-saturated, which makes the dehazed image appear darker (i.e., the color tone of the river, airport ground, plants, roads appear bit dark for both QUICK-BIRD [41] and PLEIADES dataset [43], whereas serious color-distortion exist for the SIPI dataset [44]). It happens because Fu et al. [5] method is based on the principle of histogram equalization, which has an inherent problem of over-saturation. Kwok et al. [11] results in Figs. 6(c)–8(c), are comparatively clear as the method removes the

haze effect and highlighted well the details of ground infrastructures. Moreover, the bluish cast has been removed in the SIPI dataset [44]), but flaws can be seen around some water regions (i.e., the color tone of the water changed to dark).

He et al. [13] results, shown in Figs. 6(d)–8(d) are slightly over-saturated, because of incorrect transmission and air-light estimation, which is the key for efficient dehazing. Zhu et al. [20] produces results similar to those of He et al. [13] in Fig. 6(e)–8(e). However, colors are over-saturated, for example colors are bit dark in the QUICK BIRD [41] and PLEIADES dataset [43], whereas the method fails to unveil detail in USC-SIPI dataset [44]. As shown in Figs. 6(f)–8(f), Meng et al. [23], dehazing results are satisfactory, and scene-information is recovered well without any visual-artifact. However, by looking closer, we find that there exist a thin layer of haze in the QUICK BIRD [41] and PLEIADES dataset [43], and serious color-distortion exist for the USC-SIPI dataset [44].

It can be observed from Fig. 6[(g)–(i)] to Fig. 8[(g)–(i)], that learning based methods, such as [25,28], and [29] tends to either over dehaze or under dehaze the image, making the results darker or leaving haze residuals in the output. It can be evidenced by the results in Figs. 6(g)–8(g), where Cai et al. [25] method tends to produce dark regions in the QUICK BIRD [41] and PLEIADES dataset [43], and leave some haze residuals in the USC-SIPI dataset [44]. It is easy to notice that Zhang et al. [28] dehazing results in Figs. 6(h)–8(h), tends to over-amplify the intensity and thus produces exaggerated contrast and color-fringing artifacts in some regions (i.e., soil field in both QUICK BIRD [41] and PLEIADES dataset [43] is difficult to visualize). Likewise others, Zhang et al. [28] method cannot handle the problem of atmospheric color-cast in USC-SIPI dataset [44] and results in color fringing artifacts.

Our dehazing results in Figs. 6(j)–7(j) are closer to Yang et al. [29] results. Though Yang's method improve the contrast and visibility in the QUICK BIRD [41] and PLEIADES dataset [43], it shows serious color-distortion for the USC-SIPI dataset [44]. In contrast, our method recovers the scene information in all three dataset [41,43,44]. It can be seen in Figs. 6(j)–8(j) that restored images have more information, and well-enhanced edges. Our method not only improves visibility by

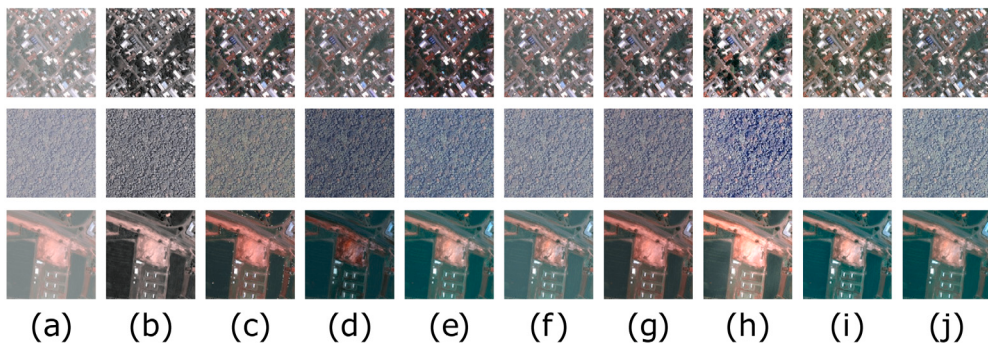


Fig. 7. Qualitative comparison with other state-of-the-art methods on PLEIADES dataset [43]. (a) Satellite haze images. (b) Fu et al. [5] (c) Kwok et al. [11] (d) He et al. [13] (e) Zhu et al. [20] (f) Meng et al. [23] (g) Cai et al. [25] (h) Zhang et al. [28] (i) Yang et al. [29] (j) Proposed method (Please zoom-in for better illustration of minor details). (For interpretation of the references to colour in this figure legend, the reader is referred to the web version of this article.)

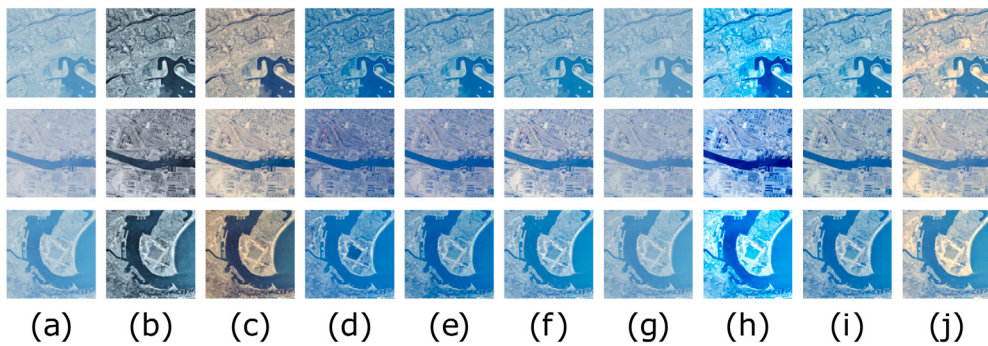


Fig. 8. Qualitative comparison with other state-of-the-art methods on USC-SIPI dataset [44]. (a) Satellite haze images. (b) Fu et al. [5] (c) Kwok et al. [11] (d) He et al. [13] (e) Zhu et al. [20] (f) Meng et al. [23] (g) Cai et al. [25] (h) Zhang et al. [28] (i) Yang et al. [29] (j) Proposed method (Please zoom-in for better illustration of minor details). (For interpretation of the references to colour in this figure legend, the reader is referred to the web version of this article.)

brightening the dark areas but also preserves the natural appearance, which unveils more details.

5.4. Qualitative comparison on synthetic haze images

The qualitative evaluation of the proposed method with the other state-of-the-art methods [5,11,13,20,23,25,28,29] is also tested on synthetic haze images. Fig. 9(a) shows some synthetic haze images, which are synthesized from clear images by randomly chosen air-light $A = 0.9$ and $\beta = 1.8$. However, these simulated haze images still have some differences from real UAVs images. Fig. 9[(b)-(i)] shows the results of Fu et al. [5], Kwok et al. [11], He et al. [13], Zhu et al. [20], Meng et al. [23], Cai et al. [25], Zhang et al. [28] and Yang et al. [29], respectively. The result of proposed method are given in Fig. 9(j) and (k) shows the ground-truth for comparison. The reader is urged to zoom into the marked regions in Fig. 9 to see the haze removal effect by each method. It can be seen from the results in Figs. 9(b)-(c) that IE methods, such as [5–11], fail to obtain the genuinely haze-free images and their results contain haze residuals compared to ground truth images. It happens because IE methods [5–11] are not primarily designed for dehazing, and they usually fail under such hazy conditions.

On the contrary, the traditional prior based methods such as [13, 20], and [23] can effectively remove the haze effect. However, visibility, colors, and brightness are not good enough, and their dehazing results contain darkness and color-distortion compared to ground truth images. As observed in Fig. 9(d), He et al. [13] method cannot handle gloomy and white objects and tend to produce severe halo-artifacts and color-distortion when the intensity of any bright object becomes similar to the intensity of air-light (see the marked region for detail difference). Zhu et al. [20], results are visually satisfactory, and there are no halo-artifact. However, color distortion appears, especially in the third and fourth image of Fig. 9(e) (i.e., the colors of a chandelier, table items,

and paper turned to dark). It can be observed in Fig. 9(f) that Meng et al. [23], produces naturally-looking results without sacrificing much fidelity of the colors and textures.

Based on the deep-learning framework, Cai et al. [25] method succeeded in dealing over-saturation problem. However, the dehazing result in Fig. 9(g) still contains hazy residuals due to the imperfect estimation of haze thickness at a distance. As shown in Fig. 9(h) Zhang et al. [28] method improves contrast and unveil details via exaggerating the intensity. However, it produces considerable over-saturated results by removing haze at the price of unrealistic visual artifact (for instance marked region appears too brighter than it should be). Fig. 9(i) shows that Yang et al. [29] results are the most competitive compared to ground truth images. However, by looking closer, it can be observed that slight color-distortion and over-enhanced regions exist (see the chandelier, colors of table items in the third image and rear wall in the fourth image). In contrast, the results of the proposed method are neither over-enhanced nor under-enhanced, and even more natural and detailed than the other results.

5.5. Quantitative comparison

To quantitatively evaluate the restoration efficacy of each compared method, two full-reference image quality assessment metrics (FR-IQA), namely, PSNR-HVS-M [46], and FSIM [47] have been used. The PSNR-HVS-M [46] is an extension of commonly used PSNR that takes HVS properties such as contrast sensitivity (CS) and visual masking (VM) into account. The FSIM [47] is an improvement over SSIM by additionally taking phase congruency (PC) and gradient magnitude (GM). Since the restored images tend to have rich details than the original haze images, it is considered that the higher the value of PSNR-HVS-M [46], and FSIM [47] better is the efficacy.

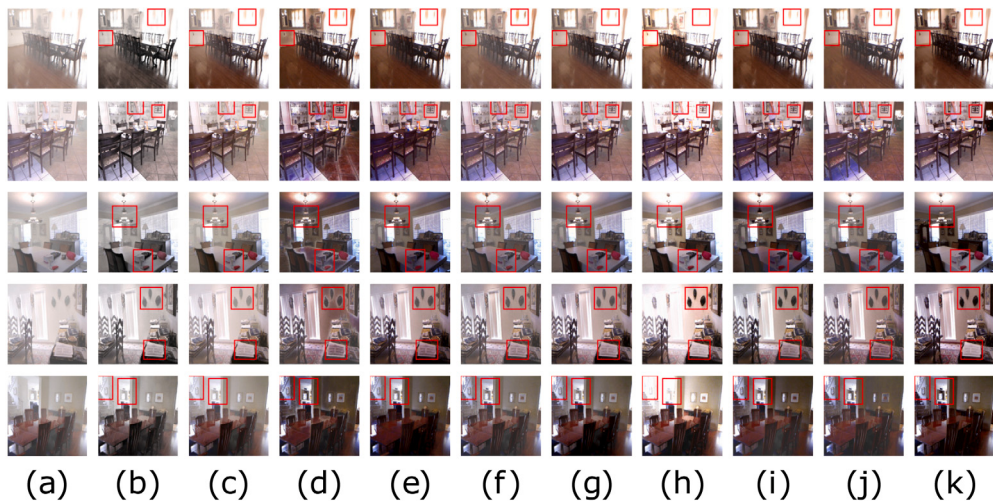


Fig. 9. Qualitative comparison with other state-of-the-art methods on RESIDE- β dataset [45]. (a) Synthetic haze images. (b) Fu et al. [5] (c) Kwok et al. [11] (d) He et al. [14] (e) Zhu et al. [20] (f) Meng et al. [23] (g) Cai et al. [25] (h) Zhang et al. [28] (i) Yang et al. [29] (j) Proposed method (k) Ground truth (Please zoom-in for better illustration of minor details in the marked region).

Table 1
Terrestrial image and UAVs image data-set.

Data-set	[48]	[49]	[50]	[51]	Total
Sizes	6033	1204	800	2100	10137

Table 2 displays the average score of each method on synthetic RESIDE- β dataset [45] with different haze level. In **Table 1**, three set of synthetic haze image (light, medium, and dense) are simulated using Eq. (1). In **Table 1**, last row corresponds to the average evaluation values of the results shown in **Fig. 9**. The results depicts the quality of the restoration directly. As shown in **Table 1**, learning based methods such as Cai et al. [25], and Yang et al. [29] outperform earlier IE methods [5]- [11] and traditional prior based IR methods [14,20], and [23] in terms of both PSNR-HVS-M, and FSIM values, respectively.

In **Table 2**, for light-haze, Cai et al. [25] stands out among the compared methods in terms of both PSNR-HVS-M and FSIM values. However, for the medium and dense haze, the results of Cai et al. [25] becomes less consistent as there still remains a thin haze residual. The proposed method shows competitive performance with Yang et al. [29] for medium and dense haze, and obtains the highest score because Yang's method produces slightly over-saturated images, while the proposed method does not. By given PSNR-HVS-M [46], and FSIM [47] results for different haze level, it can be observed that the proposed dehazing method works well and produces a natural result consistent with human observation.

To showcase the computational complexity, the average run-time comparison with other state-of-the-art methods is given in **Table 3**. The hardware specification of the computing platform are PC with Intel® Core™ i7-3770 CPU@ 3.40 GHz, 3401 MHz, 4Core(s), 8GB RAM and NVIDIA® GeForce™ GTX 1050 Ti. All methods are implemented in

Table 2
Quantitative comparison using FR-IQA metrics on synthetic reside- β data-set with different haze level.

β	Metrics	Fu et al. [5]	Kwok et al. [11]	He et al. [14]	Zhu et al. [20]	Meng et al. [23]	Cai et al. [25]	Zhang et al. [28]	Yang et al. [29]	Proposed
$\beta = [0.6, 0.9]$	PSNR-HVS-M	15.35	13.10	15.72	17.58	16.35	21.06	13.87	17.86	18.00
	FSIM	0.95	0.94	0.93	0.93	0.96	0.96	0.93	0.96	0.96
$\beta = [1.0, 1.4]$	PSNR-HVS-M	12.80	10.66	14.95	17.22	14.13	17.24	13.66	17.67	17.92
	FSIM	0.93	0.91	0.91	0.92	0.94	0.95	0.94	0.95	0.95
$\beta = [1.5, 1.8]$	PSNR-HVS-M	11.49	9.44	14.36	15.66	12.74	14.98	10.72	16.46	17.01
	FSIM	0.91	0.89	0.90	0.92	0.93	0.94	0.90	0.94	0.94

Table 3
Average run-time comparison with other state-of-the-art methods.

Methods	Run-time (seconds)	Conditions
Fu et al. [5]	0.77	Independent approach (It does not require any time for air-light estimation, transmission-map estimation, transmission-map refinement, and radiance recovery.)
Kwok et al. [11]	1.41	–
He et al. [14]	8.91	Took 0.02, 0.11, 8.74, 0.04 sec for each step.
Zhu et al. [20]	0.5	Took 0.02, 0.18, 0.29, 0.04 sec for each step.
Meng et al. [23]	4.99	Took 0.39, 0.11, 4.46, 0.03 sec for each step.
Cai et al. [25]	3.65	Took 0.02, 3.29, 0.31, 0.03 sec for each step.
Zhang et al. [28]	0.23	Jointly estimate the air-light, transmission-map, and scene radiance.
Yang et al. [29]	2.45	Jointly estimate the air-light, transmission-map, and scene radiance.
Proposed method	5.6	Took 0.02, 0.11, 5.44, 0.03 sec for each step

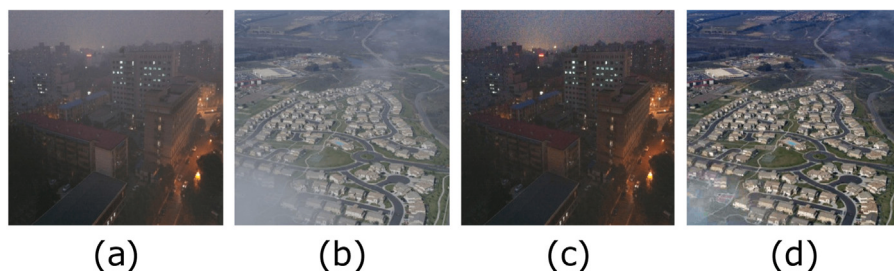


Fig. 10. Failure examples of the proposed method. (a) and (b) Input image. (c) and (d) Output image.

MATLAB R2019a under 64-bit OS (Microsoft® Windows™ 10 Pro), except Zhang et al. [28], which uses Linux with PyTorch. The results are obtained by running each method on RESIDE- β dataset [45] and taking their average. It has been observed in Table 2 that Zhang et al. [28] method is relatively fast, owing to the use of Linux and PyTorch platform. The proposed method takes more time for the refinement of transmission-map, and it can be improved by programming and using an advance computing device, such as a Graphics Processing Unit (GPU).

5.6. Discussion

UAVs images are influenced to some extent by unfavorable atmospheric conditions at the time of its acquisition. While the proposed method can effectively mitigate the effects of uniform haze between the UAVs camera and the ground, it still has some limitations. Firstly, the proposed method does not work well for night-time haze as there is not enough reflectance region in the captured image. Secondly, when there is an inconsistent haze (i.e., when air-light density is higher on one side and lower on the other side), the assumption of uniform air-light does not hold, which leads to the under-estimation of haze concentration, and makes the results hazy. Fig. 10 shows an examples, where the proposed method fails to generate the clear image. This is mainly because haze imaging model does not hold true for such situations. To address the problem of night-haze, advanced imaging model such as [52,53], and [54] need to be considered. However, the problem of non-uniform haze is still a challenge and yet to be addressed by the researchers.

6. Conclusion

In this paper, we propose an assumption based novel visibility restoration scheme for single unmanned aerial vehicle system images. The proposed method uses an assumption that actual radiance of an aerial image is bounded within the range $[C_0 \leq J^e(x) \leq C_1]$. Based on this assumption, boundary constraint utilizing the median filter have been imposed on the color channel for the rough estimation of transmission-map. Furthermore, a graph model inspired by the assumption that pixels sharing the same appearance must be expected to share the same transmission value has been used to refine the transmission-map. The experimental results with other state-of-the-art methods demonstrates that the proposed method produces high-quality, detailed images with minimal artifact and gives the best score in terms of full-reference image quality assessment metrics. For future work, we intend to address the above mentioned limitations of the proposed method.

Declaration of competing interest

The authors declare that they have no known competing financial interests or personal relationships that could have appeared to influence the work reported in this paper.

References

- [1] J.N. Hird, A. Montaghi, G.J. McDermid, J. Kariyeva, B.J. Moorman, S.E. Nielsen, A.C.S. McIntosh, Use of unmanned aerial vehicles for monitoring recovery of forest vegetation on petroleum well sites, *Remote Sens.* 9 (5) (2017).
- [2] E.R. Hunt, M. Cavigelli, C.S.T. Daughtry, J.E. McMurtrey, C.L. Walthall, Evaluation of digital photography from model aircraft for remote sensing of crop biomass and nitrogen status, *Precis. Agric.* 6 (4) (2005) 359–378.
- [3] C.A. Vanegas, D.G. Aliaga, B. Benes, P. Waddell, Visualization of simulated urban spaces: Inferring parameterized generation of streets, parcels, and aerial imagery, *IEEE Trans. Vis. Comput. Graphics* 15 (3) (2009) 424–435.
- [4] H. Lidong, Z. Wei, W. Jun, S. Zebin, Combination of contrast limited adaptive histogram equalisation and discrete wavelet transform for image enhancement, *IET Image Process.* 9 (10) (2015) 908–915.
- [5] X. Fu, J. Wang, D. Zeng, Y. Huang, X. Ding, Remote sensing image enhancement using regularized-histogram equalization and DCT, *IEEE Geosci. Remote Sens. Lett.* 12 (11) (2015) 2301–2305.
- [6] J.H. Jang, S.D. Kim, J.B. Ra, Enhancement of optical remote sensing images by subband-decomposed multiscale retinex with hybrid intensity transfer function, *IEEE Geosci. Remote Sens. Lett.* 8 (5) (2011) 983–987.
- [7] C.-T. Shen, W.-L. Hwang, Color image enhancement using retinex with robust envelope, in: 2009 16th IEEE International Conference on Image Processing, ICIP, 2009, pp. 3141–3144.
- [8] S. Huang, F. Cheng, Y. Chiu, Efficient contrast enhancement using adaptive gamma correction with weighting distribution, *IEEE Trans. Image Process.* 22 (3) (2013) 1032–1041.
- [9] K.V. Asari, E. Ogsulu, S. Arigela, Nonlinear enhancement of extremely high contrast images for visibility improvement, in: P.K. Kalra, S. Peleg (Eds.), *Computer Vision, Graphics and Image Processing*, Springer Berlin Heidelberg, Berlin, Heidelberg, 2006, pp. 240–251.
- [10] Y. Du, B. Guindon, J. Cihlar, Haze detection and removal in high resolution satellite image with wavelet analysis, *IEEE Trans. Geosci. Remote Sens.* 40 (1) (2002) 210–217.
- [11] N. Kwok, H. Shi, An integrated framework for aerial image restoration, in: 2015 International Conference on Machine Learning and Cybernetics, Vol. 1, ICMC, 2015, pp. 322–327.
- [12] P. Sidiqe, V. Sagan, M. Qumsiyeh, M. Maimaitijiang, A. Essa, V. Asari, Adaptive trigonometric transformation function with image contrast and color enhancement: Application to unmanned aerial system imagery, *IEEE Geosci. Remote Sens. Lett.* 15 (3) (2018) 404–408.
- [13] K. He, J. Sun, X. Tang, Single image haze removal using dark channel prior, *IEEE Trans. Pattern Anal. Mach. Intell.* 33 (12) (2011) 2341–2353.
- [14] J. Long, Z. Shi, W. Tang, C. Zhang, Single remote sensing image dehazing, *IEEE Geosci. Remote Sens. Lett.* 11 (1) (2014) 59–63.
- [15] Y. Cheng, W. Niu, Z. Zhai, Video dehazing for surveillance unmanned aerial vehicle, in: 2016 IEEE/AIAA 35th Digital Avionics Systems Conference, DASC, 2016, pp. 1–5.
- [16] D. Singh, V. Kumar, Dehazing of remote sensing images using fourth-order partial differential equations based trilateral filter, *IET Comput. Vis.* 12 (2) (2018) 208–219.
- [17] Y. Huang, W. Ding, H. Li, Haze removal for UAV reconnaissance images using layered scattering model, *Chin. J. Aeronaut.* 29 (2) (2016) 502–511.
- [18] X. Zhao, W. Ding, C. Liu, H. Li, Haze removal for unmanned aerial vehicle aerial video based on spatial-temporal coherence optimisation, *IET Image Process.* 12 (1) (2018) 88–97.
- [19] P. Carr, R. Hartley, Improved single image dehazing using geometry, in: 2009 Digital Image Computing: Techniques and Applications, 2009, pp. 103–110.
- [20] Q. Zhu, J. Mai, L. Shao, A fast single image haze removal algorithm using color attenuation prior, *IEEE Trans. Image Process.* 24 (11) (2015) 3522–3533.
- [21] D. Berman, T. Treibitz, S. Avidan, Non-local image dehazing, in: 2016 IEEE Conference on Computer Vision and Pattern Recognition, CVPR, 2016, pp. 1674–1682.
- [22] T.M. Bui, W. Kim, Single image dehazing using color ellipsoid prior, *IEEE Trans. Image Process.* 27 (2) (2018) 999–1009.

- [23] G. Meng, Y. Wang, J. Duan, S. Xiang, C. Pan, Efficient image dehazing with boundary constraint and contextual regularization, in: 2013 IEEE International Conference on Computer Vision, 2013, pp. 617–624.
- [24] K. Tang, J. Yang, J. Wang, Investigating haze-relevant features in a learning framework for image dehazing, in: 2014 IEEE Conference on Computer Vision and Pattern Recognition, 2014, pp. 2995–3002.
- [25] B. Cai, X. Xu, K. Jia, C. Qing, D. Tao, DehazeNet: An end-to-end system for single image haze removal, *IEEE Trans. Image Process.* 25 (11) (2016) 5187–5198.
- [26] W. Ren, S. Liu, H. Zhang, J. Pan, X. Cao, M.-H. Yang, Single Image Dehazing via Multi-Scale Convolutional Neural Networks, in: European Conference on Computer Vision, 2016.
- [27] B. Li, X. Peng, Z. Wang, J. Xu, D. Feng, AOD-Net: All-in-one dehazing network, in: 2017 IEEE International Conference on Computer Vision, ICCV, 2017, pp. 4780–4788.
- [28] H. Zhang, V.M. Patel, Densely connected pyramid dehazing network, in: 2018 IEEE/CVF Conference on Computer Vision and Pattern Recognition, 2018, pp. 3194–3203.
- [29] D. Yang, J. Sun, Proximal dehaze-net: A prior learning-based deep network for single image dehazing, in: ECCV, 2018.
- [30] Y. Du, X. Li, Recursive deep residual learning for single image dehazing, in: 2018 IEEE/CVF Conference on Computer Vision and Pattern Recognition Workshops, CVPRW, 2018, pp. 843–8437.
- [31] R. Li, J. Pan, Z. Li, J. Tang, Single image dehazing via conditional generative adversarial network, in: 2018 IEEE/CVF Conference on Computer Vision and Pattern Recognition, 2018, pp. 8202–8211.
- [32] W. Ren, L. Ma, J. Zhang, J. Pan, X. Cao, W. Liu, M.-H. Yang, Gated fusion network for single image dehazing, in: IEEE Conference on Computer Vision and Pattern Recognition, 2018.
- [33] H. Zhang, V.M. Patel, Densely connected pyramid dehazing network, in: CVPR, 2018.
- [34] A. Galdran, A. Alvarez-Gila, A. Bria, J. Vazquez-Corral, M. Bertalmio, On the duality between retinex and image dehazing, 2017, CoRR, vol. abs/1712.02754.
- [35] C.O. Ancuti, C. Ancuti, Single image dehazing by multi-scale fusion, *IEEE Trans. Image Process.* 22 (8) (2013) 3271–3282.
- [36] A. Levin, D. Lischinski, Y. Weiss, A closed-form solution to natural image matting, *IEEE Trans. Pattern Anal. Mach. Intell.* 30 (2) (2008) 228–242.
- [37] Q. Chen, D. Li, C. Tang, KNN Matting, *IEEE Trans. Pattern Anal. Mach. Intell.* 35 (9) (2013) 2175–2188.
- [38] S. Gautam, T.K. Gandhi, B.K. Panigrahi, Single image dehazing using image boundary constraint and nearest neighborhood optimization, in: Proceedings of the 11th Indian Conference on Computer Vision, Graphics and Image Processing, ICVGIP 2018, Association for Computing Machinery, New York, NY, USA, 2018.
- [39] L. Karacan, A. Erdem, E. Erdem, Alpha matting with KL-divergence-based sparse sampling, *IEEE Trans. Image Process.* 26 (9) (2017) 4523–4536.
- [40] X. Chen, D. Zou, S.Z. Zhou, Q. Zhao, P. Tan, Image matting with local and nonlocal smooth priors, in: 2013 IEEE Conference on Computer Vision and Pattern Recognition, 2013, pp. 1902–1907.
- [41] QUICKBIRD Satellite Database, 2019, [Online]. Available: <http://www.engesat.com.br/imagem-de-satelite/quick-bird/>. (accessed January 2019).
- [42] S. Gautam, T.K. Gandhi, B.K. Panigrahi, An advanced visibility restoration technique for underwater images, in: 2018 25th IEEE International Conference on Image Processing, ICIP, 2018, pp. 1757–1761.
- [43] PLEIADES Satellite Database, 2019, [Online]. Available: <http://www.engesat.com.br/imagem-de-satelite/pleiades/>. (Accessed January 2019).
- [44] USC-SIPI Satellite Database, 2019, [Online]. Available: <http://sipi.usc.edu/database/database.php?volume=aerials&image=1#top>. (Accessed January 2019).
- [45] B. Li, W. Ren, D. Fu, D. Feng, W. Zeng, Z. Wang, Benchmarking single-image dehazing and beyond, *IEEE Trans. Image Process.* 28 (1) (2019) 492–505.
- [46] N.N. Ponomarenko, F. Silvestri, K.O. Egiazarian, M. Carli, J. Astola, V.V. Lukin, On Between-coefficient contrast masking of dct basis functions, in: Proceedings of the Second International Workshop on Video Processing and Quality Metrics, Vol. 4, 2007.
- [47] L. Zhang, L. Zhang, X. Mou, D. Zhang, FSIM: A feature similarity index for image quality assessment, *IEEE Trans. Image Process.* 20 (8) (2011) 2378–2386.
- [48] P. Welinder, S. Branson, T. Mita, C. Wah, F. Schroff, S. Belongie, P. Perona, Caltech-UCSD Birds 200, Tech. Rep. CNS-TR-2010-001, California Institute of Technology, 2010.
- [49] W.S. Geisler, J.S. Perry, Statistics for optimal point prediction in natural images, *J. Vis.* 11 (12) (2011) 14.
- [50] G. Cheng, J. Han, P. Zhou, L. Guo, Multi-class geospatial object detection and geographic image classification based on collection of part detectors, *ISPRS J. Photogramm. Remote Sens.* 98 (2014) 119–132.
- [51] Y. Yang, S. Newsam, Bag-of-visual-words and Spatial Extensions for Land-use Classification, in: Proceedings of the 18th SIGSPATIAL International Conference on Advances in Geographic Information Systems, GIS '10, ACM, New York, NY, USA, 2010, pp. 270–279.
- [52] M. Yang, J. Liu, Z. Li, Superpixel-based single nighttime image haze removal, *IEEE Trans. Multimed.* 20 (11) (2018) 3008–3018.
- [53] Y. Li, R.T. Tan, M.S. Brown, Nighttime haze removal with glow and multiple light colors, in: 2015 IEEE International Conference on Computer Vision, ICCV, 2015, pp. 226–234.
- [54] J. Zhang, Y. Cao, S. Fang, Y. Kang, C.W. Chen, Fast haze removal for nighttime image using maximum reflectance prior, in: 2017 IEEE Conference on Computer Vision and Pattern Recognition, CVPR, 2017, pp. 7016–7024.